Quenching induced modified nanoarchitectonics in the dielectric and energy storage behavior of poly (vinylidene fluoride)/Ba$_{0.7}$Sr$_{0.3}$TiO$_3$ composites thick films

Pallavi Gupta[1] · Sachin Jaidka[1] · Dwijendra P. Singh[1]

Abstract

Free-standing flexible poly(vinylidene fluoride)-barium strontium titanate (PVDF-BST) composite films loaded with 5 vol% of Ba$_{0.7}$Sr$_{0.3}$TiO$_3$ submicronic particles have been synthesized. The synthesized PVDF-BST composite film was quenched in ice water as quenching strongly affects its crystalline phase, dielectric and energy storage behavior. X-ray diffraction (XRD) and Fourier transform infrared (FTIR) studies confirmed that quenching leads to the evolution of the β-phase of PVDF in the PVDF-BST composite films. At 1 kHz, the dielectric constant of the quenched film is ~ 17, which is higher than that of the unquenched film, i.e. ~ 15. At 460 kV/cm, the energy density of the quenched film is 2.5 times higher (~ 4.8 J/cc) as compared to the unquenched film (1.9 J/cc). Significant improvement in the dielectric constant and energy density is attributed to the formation of β-phase of PVDF in PVDF-BST composite film. Mechanism for β-phase formation by quenching at low temperatures has also been suggested.

Keywords Polymer-ceramic composites · Quenching technique · Dielectric constant · Energy density

1 Introduction

High energy density capacitors have currently gained a lot of interest due to their wide range of applications in defense, rail guns and high-power electronics [1–3]. The energy density of any material is given by $U = \frac{1}{2}\varepsilon_r\varepsilon_0 E_b^2$, where U is the energy density, ε_o is the vacuum permittivity, ε_r is the dielectric permittivity of the material, and E_b^2 is the breakdown strength of the material or by using the formula $U_E = \int E.dP$, where E and P refer to the electric field and polarization, respectively and U_E is the calculated energy density. Therefore, materials having high dielectric constant and high breakdown strength are required for this purpose. Many ceramics such as lead zirconium titanate (Pb(Zr$_x$Ti$_{1-x}$)O$_3$) [PZT], barium strontium titanate (Ba$_x$Sr$_{1-x}$TiO$_3$) [BST], and barium titanate (BaTiO$_3$) [BT] have high dielectric constant; but have very low breakdown strength [4, 5]. The composites of PVDF with ceramic particles like BST can be used for producing relatively high dielectric constant (~ 25) and moderate breakdown strength [6]. These composites can be used as an alternative for high energy density capacitors [4, 5, 7, 8]. Ferroelectric ceramics such as PZT or BaTiO$_3$ are preferred as dielectric materials in capacitors because of their high dielectric constant [9, 10]. However, being ferroelectric, they are defined by their high remanent and saturation polarization, both of which reduce the energy density [11, 12]. Among the various lead-free ferroelectric materials, barium strontium titanate (BST) was chosen for this study because of its very good and stable dielectric behavior. BST not only exhibits an extraordinarily giant dielectric constant at room temperature (e.g. 2500–3000) but also a nearly constant dielectric constant up to a temperature of 120 ℃, and over a wide frequency range (100 Hz to 1 MHz) [13, 14]. The non-toxic nature of BST and very good dielectric behavior place it on edge as compared to other ceramic nanofillers.

High energy density in PVDF-based composites is mostly achieved by high loading of ceramic particles. However, the high loading of ceramic particles in the PVDF matrix decreases the breakdown strength [10, 15]. Moreover, at low loading of ceramics in PVDF composites, a significant improvement in high dielectric constant and high energy

✉ Dwijendra P. Singh
dpsingh@thapar.edu

1   Energy Materials Lab, Department of Physics and Materials Science, Thapar Institute of Engineering and Technology, Patiala, Punjab 147004, India

density is reported [16, 17]. Tang et al. [16] studied the effect of the incorporation of $Ba_{0.2}Sr_{0.8}TiO_3$ nanowires into the PVDF matrix. It was observed that the energy density with 7.5% $Ba_{0.2}Sr_{0.8}TiO_3$ reached 14.86 J/cc at 450 MV/m, which represents a 42.9% increase in comparison to the PVDF which is ascribed to high aspect ratio nanowires. On the other hand, Pan et al. [17] found that the inclusion of 10.8 vol% dopamine-modified $BaTiO_3$ (BT-DA) nanotubes into the PVDF polymer matrix increased the dielectric constant to 47.05, which is ascribed to two main factors: (i) introduction of high dielectric constant BT-DA nanotubes and (ii) accumulation of a large amount of charges at the interfaces between the fillers and the matrix. The crucial factor responsible for achieving high energy density in PVDF-based composite films is the stability of the ferroelectric β-phase. The β-phase is desirable for device applications due to its good piezoelectric and ferroelectric properties since it conforms TGTG configuration of CH_2 and CF_2 dipole in PVDF [18–20]. Therefore, various ways are employed to modify the crystalline structure of PVDF in PVDF-based nanocomposites, such as stretching [11], functionalization [21], poling [22] and quenching [23]. It is well known that PVDF exists in three different crystalline forms. These are α (non-polar), β (polar), γ (polar) phases. Among the various crystalline phases of PVDF, the α-phase is most stable and commonly obtained during the synthesis of PVDF, while the β-phase of PVDF could be obtained through unusual processing such as stretching and quenching of the film [11, 23–25].

There are few reports on the quenching of the PVDF films. Tiwari et al. reported that quenching of the PVDF film in ice water leads to the formation of polar β-phase [26], while Li et al. have observed γ-phase [27]. Soin et al. [28] have investigated the effect of quenching on the crystalline structure of PVDF films. The samples have been quenched at three different temperatures, viz. 100 ℃, 0 ℃ and – 20 ℃. They have suggested that the low-temperature quenching promotes the formation of self-aligned β-phase of PVDF. Liu et al. [29] have studied the effect of quenching on the structural properties of PVDF-BST composite films. They obtained α-phase even after quenching. These investigations have not covered the influence of quenching on the structural, dielectric and energy storage behavior comprehensively. Moreover, they also lack the explanation of the phenomena causing the variation in these properties. The present study aims to investigate the quenching-induced modification in crystalline structure and its effect on the dielectric and energy storage behavior of PVDF-based composite films. Here, we report the effect of quenching in ice water on the structural, dielectric and energy storage properties of PVDF-$Ba_{0.7}Sr_{0.3}TiO_3$ (PVDF-BST) composite film. The underlying mechanism for the improved behavior has also been suggested.

2 Experimental procedure

The submicronic $Ba_{0.7}Sr_{0.3}TiO_3$ (BST) cuboid particles of (~ 100 nm) were synthesized by the sol–gel method, as reported earlier [30]. For this, a stoichiometric mixture of barium acetate ($Ba(CH_3COO)_2$; Sigma Aldrich), strontium acetate ($Sr(CH_3COO)_2$; Sigma Aldrich) and Ti(IV) isopropoxide ($TiO_4C_{12}H_{28}$; 97% Sigma Aldrich) chemicals were used as precursors. Barium acetate and strontium acetate were dissolved in acetic acid, whereas titanium isopropoxide was dissolved in 2-methoxy ethanol. The two solutions were then mixed under vigorous stirring. The resulting solution was refluxed for 2 h at 100 °C and a white powder was obtained. This white powder was then calcined at 1000 °C for 8 h to get $Ba_{0.7}Sr_{0.3}TiO_3$ (BST) cuboid particles. The PVDF powder purchased from Alfa Aesar (purity 99.8%) was used in the received condition. 2gm PVDF powder was dissolved in polar dimethylformamide (DMF) solvent and kept in an ultrasonic bath for 30 min. In the sonicated solution of PVDF and DMF, 5 vol% of BST submicronic cuboid particles were added and stirred at 50 °C for 2 h. The homogenized solution was then poured into a petri dish and then left for drying in the air for ~ 24 h. The complete evaporation of DMF was ensured by heating the petri dish in an oven at 160 ℃ for 2 h. Afterward, the petri dish was allowed to cool down in the air to get the unquenched film. Same procedure was followed to get different sets of unquenched film. For obtaining PVDF-BST quenched films, a petri dish containing film, which was prepared by heating in an oven at 160 ℃ for 2 h, was transferred immediately into a beaker containing ice cubes. The schematic of the quenching arrangement is shown in Fig. 1a. Ice cubes were placed in a beaker and a copper metal plate was kept on it to maintain temperature uniformly. A PT-100 sensor was used to measure the temperature and it was found to be ~ 3 ℃. The as synthesized film and the schematic for the electrical characterization are shown in Fig. 1b and c. The copper metal plate had a thickness of 5 mm and a diameter of 10 cm and the sample of ~ 150 μm thickness was cut into small circular pieces of diameter 15 mm. The temperature sensor was connected to a thermocouple unit, which was simply dipped into the beaker containing ice cubes and the dipping distance was up to the copper plate. This gave a temperature reading of ~ 3 ℃ at the copper plate, which acted as the quenching medium.

X-ray diffraction (XRD) spectra of PVDF-BST composite films was recorded with X′pert PROMRD (Pan Analytical) diffractometer with Cu Kα radiation (λ = 1.5460 Å). XRD was measured in the range of 10–60°. Fourier-transformed Infrared spectroscopy (FTIR) spectra were recorded using a Perkin Elmer spectrophotometer (Model

Fig. 1 Schematic of the **a** quenching arrangement, **b** as-synthesized film and **c** electrical characterization
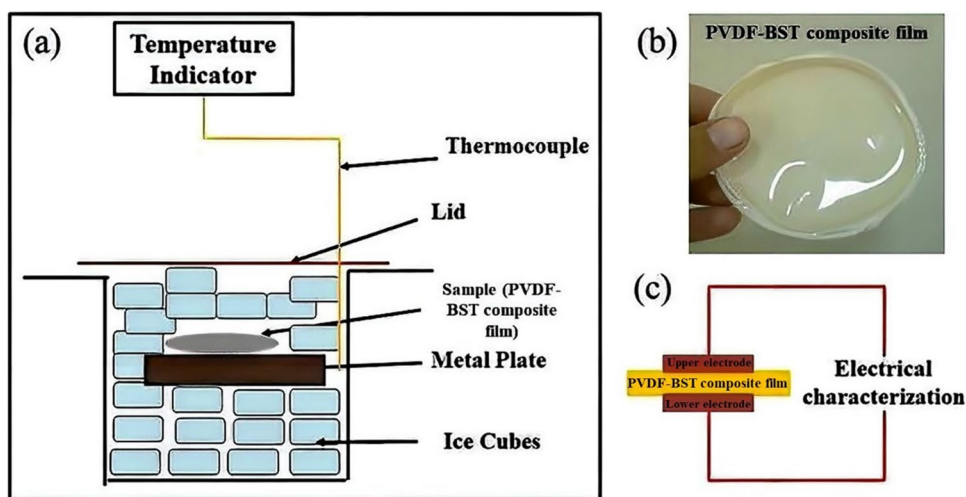
Frontier). The FTIR spectra was taken in the range of 700–1500 cm^{-1} wavenumber range for the testing purpose. Differential Scanning Calorimetry (DSC) of composite films was carried out by NETZSCH STA449C Jupiter instrument under a nitrogen atmosphere with a heating rate of 5 ℃/min. DSC was taken in the range of 80–180 ℃. For electric measurements, circular electrodes of gold having a diameter (~7 mm) were deposited on both sides of the composite films using a metal shadow mask. Dielectric properties of the composite films were measured by Hioki 353,250 LCR meter in the frequency range from 100 Hz to 1 MHz at room temperature. The unipolar polarization–electric field (P-E) loop measurements were carried out using Premier II Radiant Ferroelectric Tester by applying a triangular wave of 10 Hz frequency. The

energy storage properties were studied in the electric field range of 0 to 550 kV/cm.

3 Results and discussion

Figure 2a and b show the XRD pattern of the unquenched and quenched PVDF-BST composite films, respectively. The XRD pattern of BST matches well with JCPDS card no. 79–2263. Figure 2a shows a prominent peak at ~18.5°, corresponding to the α-phase of PVDF [31]. The inset of Fig. 2a shows the enlarged view of the XRD pattern in the range 17.5–21.5°. The inset exhibits two peaks, a more intense peak at ~18.5° and a peak of relatively low intensity at 20.7° [32]. The peak at 18.5° and 20.7° corresponds to α and β crystalline phases of PVDF, respectively [31]. Therefore,
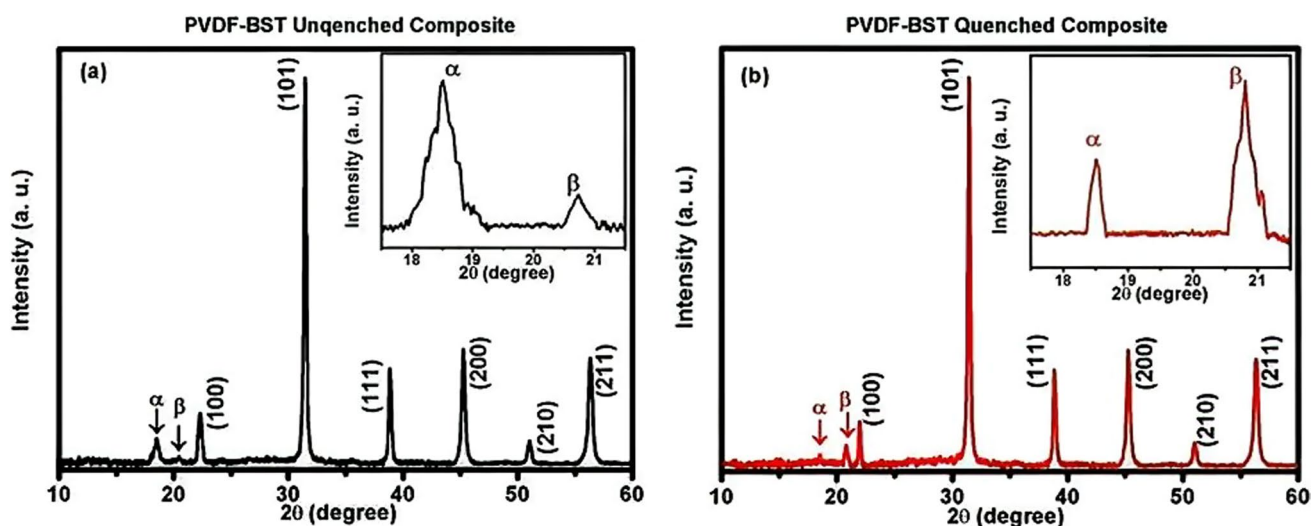

Fig. 2 X-ray diffraction of PVDF-BST composites of **a** unquenched film and **b** quenched film. Inset of Fig. 1a and b showing α and β-phase of PVDF composite films

the XRD studies indicate that the unquenched PVDF-BST film is predominantly dominated by the α-phase of PVDF.

Figure 2b shows a prominent peak at ∼ 20.7° with an inset showing the enlarged view of the XRD pattern, which shows the presence of a weak intensity peak at ∼ 18.5° along with the intense peak at ∼ 20.7°. The broadening of the peak at ∼ 20.7° (Fig. 2b) in the quenched composite film is large as compared to the peak at ∼ 18.5° (corresponding to α-phase). Therefore, the α-phase crystallites of PVDF are large as compared to β-phase. This also indicates that quenching promotes the conversion of large α-phase crystallites into smaller β-phase crystallites.

Figure 3 shows the FTIR spectra of quenched and unquenched PVDF-BST composite films. The ice water quenched PVDF-BST composite film exhibits IR absorption bands at 840, 878, 1172, and 1278 cm^{-1}, which correspond to the β-phase of PVDF [33]. The absorbance bands corresponding to the α-phase of PVDF (765 and 975 cm^{-1}) are also present [34]. The absorption bands in the range 1230–1240 cm^{-1} may either be related to β or γ-phase of PVDF, whereas the absorption band in the range of 1275–1280 cm^{-1} confirmly corresponds to β-phase of PVDF [18, 35]. On the other hand, in unquenched PVDF-BST film, the absorbance bands of α-phase (765, 795 cm^{-1}) are prominent, whereas the absorbance bands corresponding to β-phase (872, 1178 cm^{-1}) are weak. The band at 1070 cm^{-1} is attributed to the bending of C–C–C [36].

The FTIR results indicate that after quenching in ice water, the absorbance peaks of the β-phase have become stronger, as compared to the α-phase. IR studies also confirm that quenching promotes the conversion of α-phase into β-phase
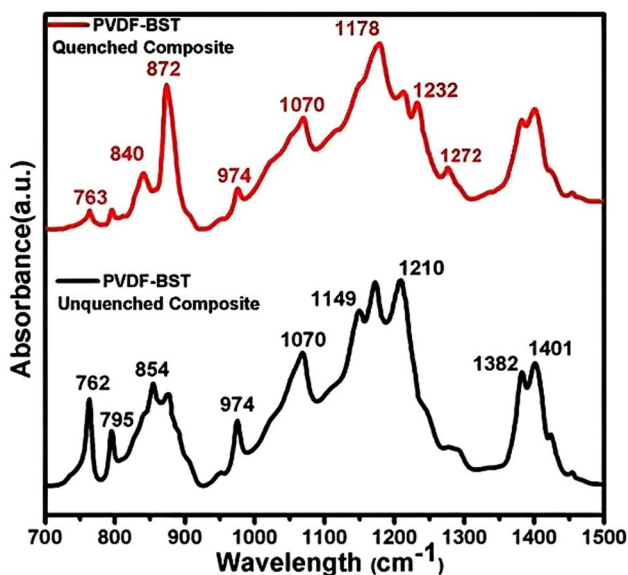
in PVDF-BST composite film. The IR studies also corroborate with the results of XRD, i.e. the quenching of PVDF-BST composite film in ice water promotes the formation of β-phase of PVDF.

Figure 4 shows the melting thermographs of quenched and unquenched PVDF-BST composite films. Both the films exhibit the melting temperature (T_m) in the temperature range of 160–165 ℃. The melting temperature of the quenched composite film in ice water is found to be ∼ 160 ℃, whereas it is ∼ 165 ℃ for the unquenched composite film. It is reported in the literature that melting of the β-phase of pure PVDF occurs in the range of 165–172 ℃, whereas α-phase and γ-phase melt in temperature ranges of 172–175 ℃ and 175–180 ℃, respectively [36, 37]. The melting temperature of composite films is usually found to be lower as compared to pure PVDF film [38] because the addition of ferroelectric ceramic filler in the polymer matrix causes a reduction in crystalline content and enhances loosely packed molecular chain structure.

The observation of lower melting temperature of quenched PVDF-BST composite film at ∼ 160 ℃ suggests that quenching enhances the formation of β-phase. The melting temperature of ∼ 165 ℃ in the unquenched composite film suggests the dominance of the α-phase of PVDF. Although DSC is not considered an important tool for deciding the crystalline phases of PVDF, but it supports XRD and IR results. The melting crystallinity X_c^m of quenched and unquenched PVDF–BST composite films based on their melting data can be obtained from the following equation:

$$X_c^m = \frac{\Delta H_m \times 100}{\Delta H_{100\%\ crystalline}}$$

where $\Delta H_{100\%\ crystalline}$ is the melting enthalpy for 100% crystalline PVDF, which is equal to 104.7 J/g [39] and ΔH_m is

Fig. 3 Fourier transform infrared spectroscopy of quenched and unquenched PVDF-BST composite films
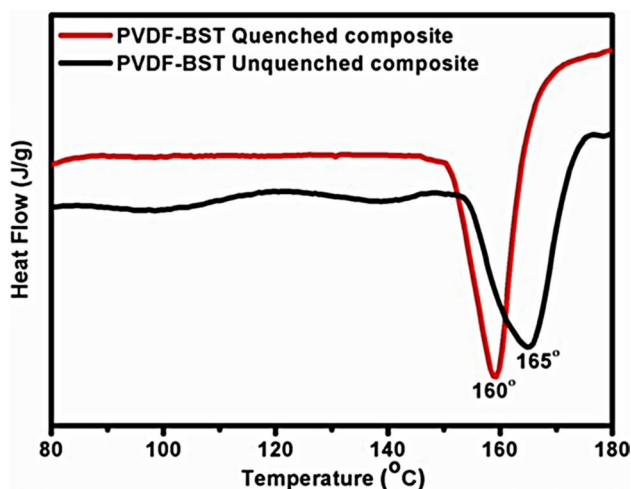

Fig. 4 DSC thermogram showing melting behavior of quenched and unquenched PVDF composite films

the melting enthalpy of the samples. The values of melting temperature (T_m), melting enthalpy (H_m) and crystallinity (X_c) are given in Table 1. The crystallinity for quenched composite film (~ 34%) has been found to be higher as compared to unquenched film. DSC result also indicates the enhancement in the β-phase of PVDF upon quenching. The increase in crystallinity for β-phase has also been observed by Buonomenna et al. [40].

The α and β crystalline phases of PVDF are non-polar and polar in nature, respectively. The strong dipole moment ($5–8 \times 10^{-30}$ Cm) of the PVDF monomer unit is caused by the large electronegativity of fluorine as compared to carbon and hydrogen atoms [41]. XRD, FTIR and DSC studies reveal the enhancement of the β-phase of PVDF in quenched film of PVDF-BST composite. Therefore, to get insight into the dipolar behavior of quenched and unquenched films, the electrical characterization at low and high fields is carried out.

Low-field studies have been carried out by measuring frequency-dependent dielectric constant and tangent loss. Figure 5a shows the frequency-dependent dielectric constant of quenched and unquenched PVDF-BST composite films. The dielectric constant for quenched PVDF-BST composite film increases over the entire frequency range as compared to unquenched film. At 1 kHz, the dielectric constant of quenched film (~ 17) is higher as compared to unquenched film (~ 15). The dielectric constant in PVDF-BST composite

film is mainly due to the Maxwell–Wagner-Sillars (MWS) interfacial polarization and space charge polarization [42, 43]. The variation of frequency-dependent dielectric constant for quenched as well as unquenched film is similar, i.e. dielectric constant decreases with frequency. At higher frequencies (> 100 kHz), the dielectric constant of all composites is found to decrease because the dipoles of fillers and PVDF cannot shift their orientation because the relaxation frequency of PVDF and ceramic filler is lower as compared to the frequency of applied electric field [44].

The high dielectric constant of quenched PVDF-BST composite film is attributed to (i) Formation of β-phase in PVDF and (ii) Formation of a large number of interfacial dipoles between β-phase of PVDF matrix and $Ba_{0.7}Sr_{0.3}TiO_3$ submicronic particles. The loss tangent for the quenched and unquenched PVDF- BST composite film is shown in Fig. 5b. The tan δ for the unquenched film is 0.024, while for the quenched film, it is 0.025 at 1 kHz. The tangent loss is mainly arising due to the combined effect of DC conductivity, interfacial polarization and dipolar relaxation [45]. High field studies are carried out by measurement of polarization with respect to electric field.

The unipolar polarization vs. electric field behavior is shown in Fig. 6. The energy behavior of PVDF-BST composite is measured by its discharge energy density and energy efficiency. The energy density is calculated from a unipolar P-E loop by using the formula $U_E = \int E.dP$, where E and P refer to the electric field and polarization, respectively and U_E is the calculated energy density [46]. Usually, the energy density is represented by $U_E = \int E.dD$; where $D = \varepsilon_o E + P$; for $P >> \varepsilon_o E$, therefore, $D \sim P$. Hence, the energy density is calculated by using the formula $U_E = \int E.dP$.

The schematic for the calculation of energy density is shown in Fig. 7, where region A shows discharge energy density, region A + B shows charge energy density and

Table 1 Crystallization parameter of the samples calculated from the DSC data

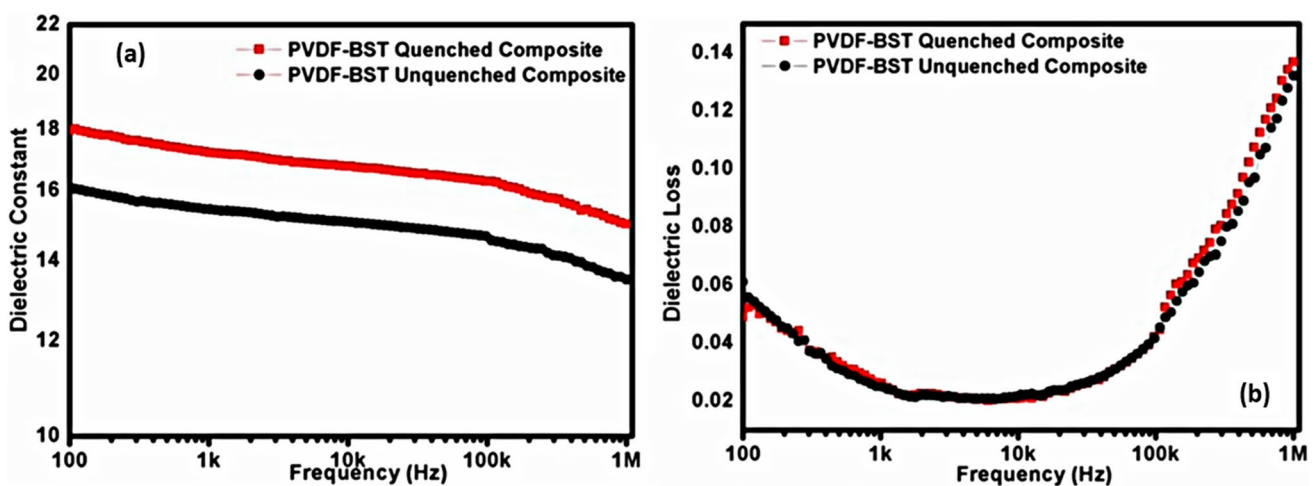| Sr. No.	T_m (℃)	X_c^m %
PVDF quenched composite	166.3	33.67
Unquenched composite	172.9	30.19

Fig. 5 Frequency dependence of **a** dielectric constant and **b** dielectric loss for PVDF-BST quenched and unquenched composite films
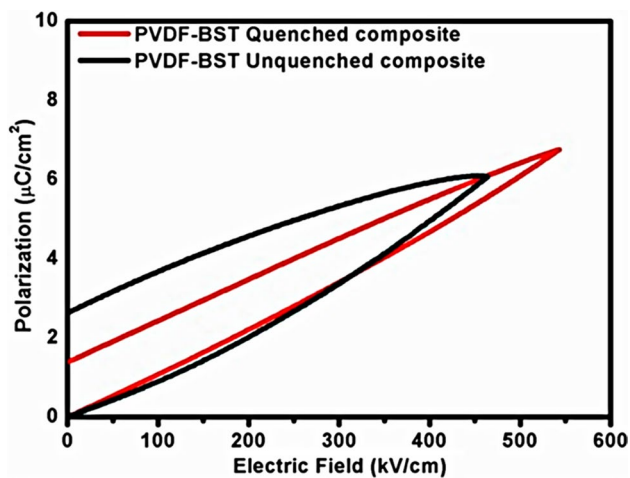
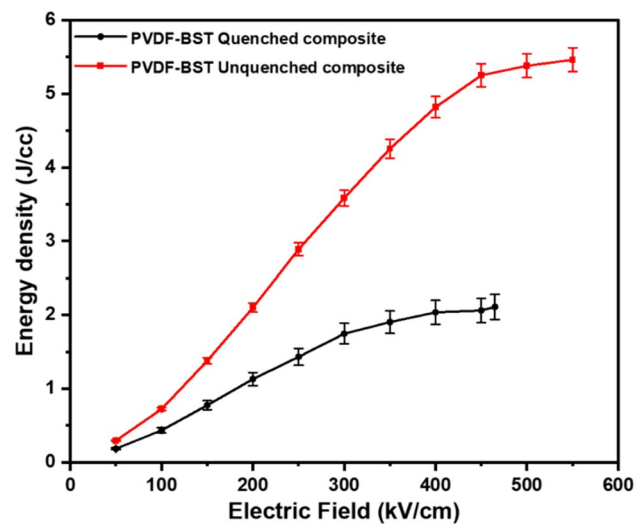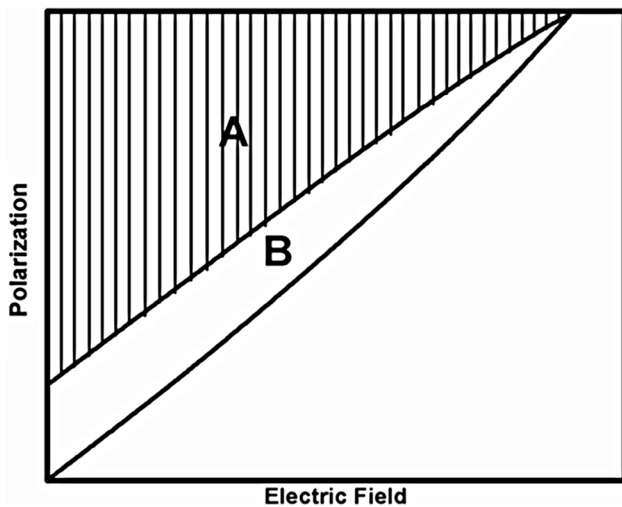**Fig. 6** Polarization vs. electric field loop for PVDF-BST quenched and unquenched composite films

Fig. 7 Schematic for the calculation of energy density

Fig. 8 Energy density vs. electric field of PVDF-BST quenched and unquenched composite films

and the polarization is easily reversible [32]. High saturation polarization at a high electric field is ascribed to the polar nature of the β-phase of quenched film. The energy density for quenched and unquenched films at 460 kV/cm is found to be 4.8 J/cc and 1.9 J/cc, respectively. Thus, the energy density for quenched PVDF-BST composite film is 2.5 times higher as compared to unquenched film. The energy efficiency for quenched and unquenched films has also been calculated by using the formula:

$$\text{Energy efficiency}(\eta\%) = \frac{\text{Discharge energy density}}{\text{Charge energy density}} \times 100\%$$

The energy efficiency for quenched and unquenched films are found to be 67% and 30.6% at 460 kV/cm, as shown in Fig. 9. The energy density as well as energy efficiency for the ice water quenched PVDF-BST composite film is higher as compared to unquenched film. Structural, dielectric, polarization and energy density studies confirm the formation of β-phase of PVDF in quenched PVDF-BST composite film. The prospective mechanism for the formation of β-phase of PVDF in PVDF-BST composite film upon quenching in ice water is described below. The error bars are denoting the error in data of energy density and efficiency at ±0.5%.

There are reports mentioning that the nucleation rate of β-phase is large as compared to α-phase at low temperatures [41, 47, 48]. Water is a polar solvent and quenching at low temperatures in ice water might promote the nucleation of β-phase. Specifically, the role of quenching of PVDF-BST composite film in water is still not clear. At low temperatures, the interaction between the -OH group of water and the –CF$_2$ group of PVDF in PVDF-BST composite film is dominant.

region B shows loss in energy density. Variations of energy density for both types of films are shown in Fig. 8. The material for high energy density must have (a) a high breakdown field, (b) high maximum polarization and (c) low remnant polarization. The respective value of maximum polarization for quenched and unquenched films is found to be 6.75 μC/cm^2 and 6.06 μC/cm^2 at an electric field of 550 kV/cm and 460 kV/cm. These values are higher for the quenched PVDF-BST composite film as compared to the unquenched film. The values of remanent polarization for quenched and unquenched films are ~ 1.40 μC/cm^2 and ~ 2.67 μC/cm^2, respectively.

Low remanent polarization of quenched film might be arising due to the smaller crystallite size of the β-phase. Smaller crystallites get polarized even at low electric field
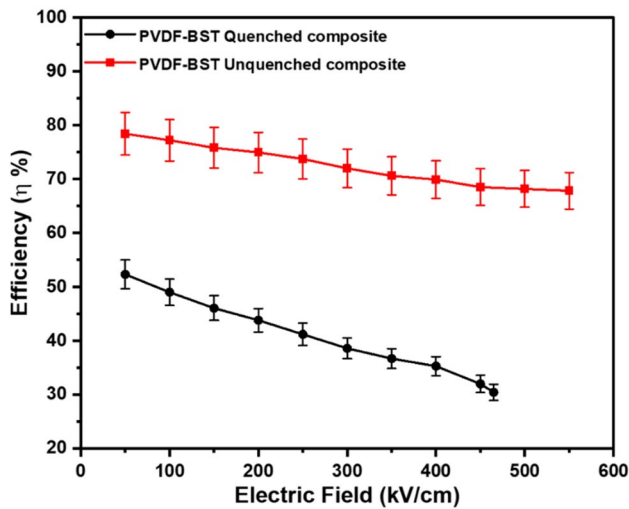
Fig. 9 Energy efficiency of PVDF-BST quenched and unquenched composite films

Immediate quenching at low temperatures in ice water induces a thermal gradient that reduces the thermal barrier [62, 63] between the –OH group of water and the –CF$_2$ group of PVDF in PVDF-BST composite film, which helps the crystal to align in the thermal field direction.

The field for β-phase alignment is originated by the development of polarizing field at the interface of the –OH group of ice water and –CF$_2$ group of PVDF by virtue of the electronegativity difference between oxygen and fluorine. The electronegativity difference leads to the formation of hydrogen bonds which in turn promotes the formation of the β-phase of PVDF in PVDF-BST composite film. The formation of β-phase is shown schematically in Fig. 10.

4 Conclusion

The effect of ice water quenching in (PVDF-BST) composite film loaded with 5 vol% of Ba$_{0.7}$Sr$_{0.3}$TiO$_3$ submicronic particles in the PVDF matrix has been investigated. Structural studies carried out by XRD, FTIR, and DSC confirm the enhancement of the β-phase of PVDF in quenched PVDF-BST composite film. Significant improvement in dielectric and energy storage behavior has also been observed. At 1 kHz, the dielectric constant of quenched film is found to be ~ 17, which is higher as compared to unquenched film ~ 15. Apart from the dielectric constant, the difference in energy density and energy efficiency is more remarkable. At an electric field of 460 kV/cm, the energy density for quenched PVDF–BST composite film is (4.8 J/cc) 2.5 times higher as compared to unquenched film (1.8 J/cc), whereas the corresponding energy efficiency is 67% and 30.6%, respectively. The increased dielectric constant and energy density is ascribed to the formation of the β-phase of PVDF in quenched PVDF-BST composite film. The formation of β-phase is attributed to the reduction in the thermal barrier, which is easily suppressed by polarizing field developed by the electronegativity difference of oxygen of -OH bond in water and fluorine of -CF$_2$ bond in PVDF. Thus, quenching at low temperatures could be a process for the development of PVDF-BST composite capacitor-grade film with enhanced dielectric and energy storage properties, which could be employed for the design of high energy density capacitors. The quenching of polymer-ceramic composite thick films has significant implications for future strategies for improving the dielectric and energy storage behavior.
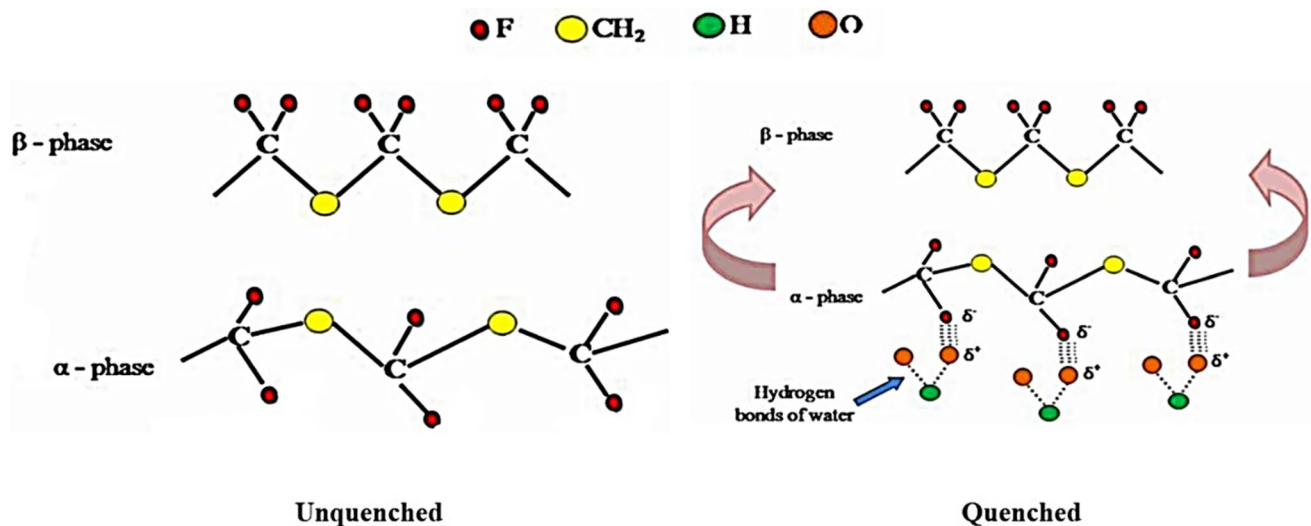

Fig. 10 Schematic diagram representing the formation of β-phase of PVDF in PVDF-BST composite film on quenching in ice water

Declarations

Conflict of interest The authors declare that they have no known conflict of interest.

References

1. F. Ali, D. Zhou, M. Ali, H.W. Ali, M. Daaim, S. Khan, M.M. Hussain, N. Sun, ACS Appl. Electron. Mater. **2**, 2301 (2020)
2. K. Yu, H. Wang, Y. Zhou, Y. Bai, Y. Niu, J Appl Phys. (2013). https://doi.org/10.1063/1.4776740
3. C. Wang, X. Zhao, L. Ren, L. Yu, Y. Jin, W. Tan, W. Zheng, H. Li, L. Yang, R. Liao, Appl Phys Lett. (2023). https://doi.org/10.1063/5.0128998
4. Y. Su, B. Zhao, Y. Wang, W. Li, P. Yuan, R. Xue, H. Wang, F. Zhang, W. Zhang, W. Zhao, Surf Interfaces **37**, 102729 (2023)
5. F. Liu, Q. Li, Z. Li, L. Dong, C. Xiong, Q. Wang, Compos. Part A Appl. Sci. Manuf. **109**, 597 (2018)
6. S. Jaidka, D.P. Singh, Polym. Compos. (2023). https://doi.org/10.1002/pc.28081
7. U. Yaqoob, A.S.M.I. Uddin, G.-S. Chung, RSC Adv. **6**, 30747 (2016)
8. E.V. Ramana, N.V. Prasad, N.M. Ferreira, A. Mahajan, I. Bdikin, M.A. Valente, F.A. Essa, B. Saleh, Surf Interfaces **33**, 102257 (2022)
9. H. Tang, Y. Lin, C. Andrews, H.A. Sodano, Nanotechnology **22**, 015702 (2010)
10. P. Kim, N.M. Doss, J.P. Tillotson, P.J. Hotchkiss, M.-J. Pan, S.R. Marder, J. Li, J.P. Calame, J.W. Perry, ACS Nano **3**, 2581 (2009)
11. S. Debili, A. Gasmi, M. Bououdina, Appl Phys A Mater Sci Process **126**, 1–9 (2020).
12. J. Claude, Y. Lu, Q. Wang, Appl Phys Lett. (2007). https://doi.org/10.1063/1.2816327
13. X. Lu, L. Zhang, Y. Tong, Z.Y. Cheng, Compos. B Eng. **168**, 34 (2019)
14. S. Jaidka, S. Chopra, A. Aggarwal, D.P. Singh, J. Phys. Chem. Solids **184**, 111667 (2024)
15. W. Xia, Z. Xu, F. Wen, Z. Zhang, Ceram. Int. **38**, 1071 (2012)
16. H. Tang, H.A. Sodano, Nano Lett. **13**, 1373 (2013)
17. Z. Pan, L. Yao, J. Zhai, B. Shen, H. Wang, Compos. Sci. Technol. **147**, 30 (2017)
18. Y. Bormashenko, R. Pogreb, O. Stanevsky, E. Bormashenko, Polym. Test. **23**, 791 (2004)
19. S. Ramasundaram, S. Yoon, K.J. Kim, J.S. Lee, Macromol. Chem. Phys. **209**, 2516 (2008)
20. J. Wu, X. Sun, S. Zhu, J. Bai, X. Zhu, J. Dai, L. Yin, W. Song, Y. Sun, Appl. Phys. A **126**, 1 (2020)
21. S. Kaur, D.P. Singh, J Alloys Compd **918**, 165500 (2022)
22. S. Jaidka, A. Aggarwal, S. Chopra, D.P. Singh, J. Electron. Mater. **51**, 5429 (2022)
23. H.L. Zhang, Q. Fu, W.P. Li, Adv Mat Res **721**, 113 (2013)
24. L. Li, M. Zhang, M. Rong, W. Ruan, RSC Adv. **4**, 3938 (2014)
25. C.-H. Du, B.-K. Zhu, Y.-Y. Xu, J. Mater. Sci. **41**, 417 (2006)
26. V. Tiwari, G. Srivastava, J. Polym. Res. **21**, 1 (2014)
27. W. Li, Q. Meng, Y. Zheng, Z. Zhang, W. Xia, Z. Xu, Appl. Phys. Lett. **96**, 10 (2010)
28. N. Soin, D. Boyer, K. Prashanthi, S. Sharma, A.A. Narasimulu, J. Luo, T.H. Shah, E. Siores, T. Thundat, Chem. Commun. **51**, 8257 (2015)
29. S. Liu, S. Xue, W. Zhang, J. Zhai, G. Chen, Ceram Int. **41**, 430–434 (2015)
30. P. Gupta, A. Kumar, M. Tomar, V. Gupta, D.P. Singh, J. Mater. Sci. Mater. Electron. **28**, 11806 (2017)
31. E. Gutiérrez-Fernández, J. Sena-Fernández, E. Rebollar, T.A. Ezquerra, F.J. Hermoso-Pinilla, M. Sanz, O. Gálvez, A. Nogales, Polymer (Guildf) **264**, 125540 (2022)
32. J. Li, Q. Meng, W. Li, Z. Zhang, J. Appl. Polym. Sci. **122**, 1659 (2011)
33. L. Yu, P. Cebe, Polymer (Guildf) **50**, 2133 (2009)
34. A.K. Zak, W.C. Gan, W.H.A. Majid, M. Darroudi, T.S. Velayutham, Ceram. Int. **37**, 1653 (2011)
35. H. Yang, Q. Wu, H. Liang, L. Wan, Z. Xu, J Polym Sci B Polym Phys **51**, 1438 (2013)
36. S. Lanceros-Mendez, J.F. Mano, A.M. Costa, V.H. Schmidt, J Macromol Sci, Part B **40**, 517 (2001)
37. B.-E. El Mohajir, N. Heymans, Polymer (Guildf) **42**, 5661 (2001)
38. M.Y.F. Elzayat, S. El-Sayed, H.M. Osman, M. Amin, Polym. Eng. Sci. **52**, 1945 (2012)
39. K. Nakagawa, Y. Ishida, J. Polym. Sci. Polym. Phys. Ed. **11**, 2153 (1973)
40. M.G. Buonomenna, P. Macchi, M. Davoli, E. Drioli, Eur. Polym. J. **43**, 1557 (2007)
41. P. Martins, A.C. Lopes, S. Lanceros-Mendez, Prog. Polym. Sci. **39**, 683 (2014)
42. T. Mizutani, T. Nagata, M. Ieda, J. Phys. D Appl. Phys. **17**, 1883 (1984)
43. W. Ou-Yang, M. Weis, X. Chen, T. Manaka, M. Iwamoto, J Chem Phys. (2009). https://doi.org/10.1063/1.3212945
44. J. Li, J. Claude, L.E. Norena-Franco, S. Il Seok, Q. Wang, Chem Mater. **20**, 6304 (2008)
45. Y. Li, X. Huang, Z. Hu, P. Jiang, S. Li, T. Tanaka, ACS Appl. Mater. Interfaces **3**, 4396 (2011)
46. Y. Song, Y. Shen, P. Hu, Y. Lin, M. Li, C.W. Nan, Appl Phys Lett. (2012). https://doi.org/10.1063/1.4760228
47. S. Chen, X. Li, K. Yao, F.E.H. Tay, A. Kumar, K. Zeng, Polymer (Guildf) **53**, 1404 (2012)
48. B.J. Rodriguez, S. Jesse, S.V. Kalinin, J. Kim, S. Ducharme, V.M. Fridkin, Appl Phys Lett. (2007). https://doi.org/10.1063/1.2715102